Engineering Transactions, **73**(3): 441–461, 2025, https://doi.org/10.24423/engtrans.3518.2025
Institute of Fundamental Technological Research Polish Academy of Sciences (IPPT PAN)
Université de Lorraine • Poznan University of Technology

SiMRTRANS

Dynamic Eccentricity Modeling of a Switched Reluctance Motor

Jakub LORENCKI*, Adrian CHMIELEWSKI

Faculty of Automotive and Construction Machinery Engineering
Warsaw University of Technology
Warsaw, Poland; e-mail: adrian.chmielewski@pw.edu.pl

*Corresponding Author e-mail: jakub.lorencki@pw.edu.pl

The switched reluctance motor (SRM), known for its robust and simple construction, is widely utilized in critical applications. This study investigates the impact of rotor dynamic eccentricity on the motor's current signal. Our research introduces a straightforward diagnostic method to detect and quantify dynamic eccentricity by analyzing the current signal spectrum. This approach specifically focuses on identifying amplitude increases in characteristic additional harmonics, leveraging fundamental electromagnetic transformations to eliminate the need for complex algorithms. Through coupled computer simulations, combining a finite element analysis model (FEMM, *Finite Element Method Magnetics* software) with dynamic equation solutions in Simulink, this study identifies specific eccentricity ranges and their corresponding characteristic current values, offering a reliable tool for SRM condition monitoring.

Keywords: switched reluctance motor; SRM; motor diagnostics; eccentricity.

Copyright © 2025 The Author(s).
Published by IPPT PAN. This work is licensed under the Creative Commons Attribution License CC BY 4.0 (https://creativecommons.org/licenses/by/4.0/).

1. Introduction

The switched reluctance motor (SRM) is a robust and reliable electric machine, making it highly suitable for demanding drive system applications. Its design is characterized by simplicity and durability, utilizing salient poles made of electric steel in both the stator and rotor, with the complete absence of windings or permanent magnets (Fig. 1). These features not only enable SRMs to achieve high rotational speeds, often exceeding 30 000 rpm [1], but also grant them high resistance to elevated temperatures and electromagnetic pulses. Consequently, SRMs are a viable and preferred choice in critical sectors such as the military, heavy machinery, and mining equipment, where reliability is paramount [2].

Consequently, effective condition monitoring of SRMs is vital to prevent potential failures and ensure their continued reliability. Among the significant is-

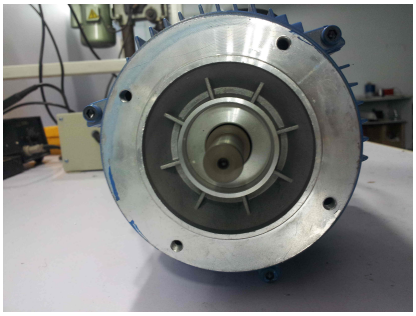

Fig. 1. SRM of 8/6 configuration designed for tests.

sues affecting such electrical motors is dynamic eccentricity, a phenomenon that often contributes to common motor faults such as bearing failures or shaft imbalances [3].

Despite the critical nature of SRM reliability, studies specifically addressing dynamic eccentricity in these motors remain relatively limited. This research gap is partly attributed to the limited market penetration of reluctance motors, which are typically found in strategic or niche applications. While diagnostic techniques for of similar effects are well-established in commonly utilized machines such as induction and synchronous motors [4], existing analyses concerning reluctance motors primarily focus on a narrow spectrum of computer-based research. These studies often address power converter-related faults, such as modified current detection [5], or explore specific applications and methodologies, for instance, soft-switching operation [6], high-resistance connection fault diagnostics [7], and niche cases in electric vehicles such as in-wheel motors under regenerative braking conditions [8] or motor geometry optimization [9]. Notably, the authors' previous works have also contributed to this field by exploring diagnostic methods for SRM dynamic eccentricity through modeling and experimental approaches [10, 11].

Early investigations into air-gap eccentricity often utilized magnetostatic field analysis to understand its influence on motor's magnetic properties. For example, Torkaman and Afjei [12] conducted a comprehensive magnetostatic field analysis to diagnose mixed eccentricity faults, elucidating their impact on magnetic field distribution and suggesting magnetic signature analysis for fault detection. Similarly, Faiz and Pakdelian [13] explored the use of mutually induced voltages as a diagnostic criterion for static eccentricity, demonstrating its significant effect on mutual flux and voltage characteristics through finite element analysis. Beyond magnetic field and voltage-based analysis, vibration-based methods have also proven effective. Dorrell and Cossar [14], for example, developed a condition monitoring system utilizing vibration measurements and harmonic analysis to detect and distinguish between static and dynamic

rotor eccentricity in SRMs. More recently, researchers have employed transient finite element methods and experimental validation to develop non-invasive diagnostic signatures. Torkaman, Afjei, and Yadegari [15], for instance, proposed an approach based on the analysis of current patterns to precisely determine the characteristic type, location of static, dynamic, and mixed eccentricity faults. These diverse methodologies underscore ongoing efforts to develop robust and reliable techniques for detecting air-gap eccentricity in SRMs.

Building upon this existing knowledge and the foundational work presented in [10, 11], the research presented in this paper aims to develop a straightforward and robust method for detecting dynamic eccentricity in SRMs by analyzing the characteristics of motor current harmonics. While previous studies, including our own work [10], have focused on foundational aspects of dynamic eccentricity and initial modeling, this paper extends these findings by providing a comprehensive analysis of the current signal spectrum across various eccentricity levels. Specifically, it identifies specific amplitude increases in characteristic harmonics, and establishes a direct relationship between eccentricity severity and current signal modulation. Furthermore, this study delves deeper into the changes in key electromagnetic parameters (flux linkage, inductance, electromagnetic torque, and co-energy) to precisely characterize the fault's impact beyond just current waveform analysis alone. This approach allows for the diagnosis of the phenomenon based solely on observing amplitude modulation effects, thus avoiding the need for complex analyses or algorithms. To achieve this, the cross-section of the reluctance motor was modeled using the finite element method magnetics (FEMM) software for each rotation angle, in both healthy and faulty (with dynamic eccentricity) conditions. The results from this static FEM analysis were then integrated into dynamic equations within Simulink, enabling the simulation of current waveforms over time and ultimately verifying the final impact of the introduced eccentricity on the motor signal.

This paper is methodically structured as follows: Sec. 2 provides an overview of the key electromagnetic properties essential for the model implementation, followed by a detailed description of the motor model under both healthy and dynamic eccentricity fault conditions. Subsequently, the analysis results are presented. Finally, Sec. 3 summarizes the research findings and outlines proposals for future work in this field.

2. Principle of operation and modeling

2.1. Motor operating principle

The SRM operates on the principle of electromagnetic torque generation, which results from the controlled modification of the magnetic flux path's per-

meance (and consequently its reluctance) by excitation of the stator windings acting on an unwound rotor. The motor's inherent asymmetry, defined by distinct salient poles on both the stator and rotor, facilitates continuous changes in magnetic flux. These unique characteristics position the SRM as a strong competitor to other DC and AC electric motors in applications requiring variable speed or servo control. However, SRMs are associated with certain drawbacks, primarily significant torque ripple and acoustic noise. These challenges stem from the double salient pole arrangement and the inherent stepwise nature of torque generation within independently controlled phases.

2.2. Motor modeling assumptions

The core of this research involved developing a simulation model of the SRM to investigate the effects of dynamic rotor eccentricity on the current signal under ideal conditions. Due to the nonlinear magnetization characteristics of the electrical steel used in the reluctance motor (Fig. 2), the motor's electrical circuit equations are inherently nonlinear and cannot be solved analytically. This limitation necessitated the development of a coupled model, integrating the FEM with dynamic equation simulations.

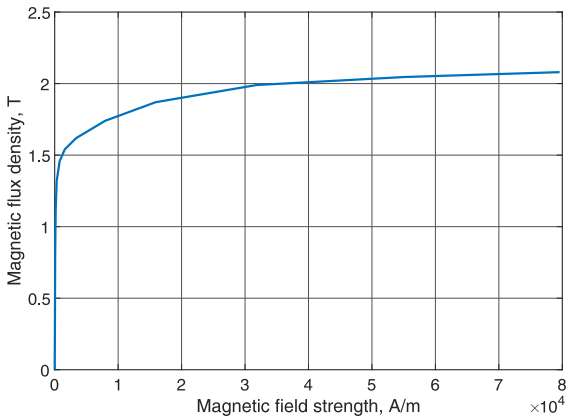

Fig. 2. Magnetization characteristics of M-19 electrical steel used in the stator and rotor.

This coupled approach enables precise determination of the magnetic flux as a function of rotor rotation angle for various current values. The resulting three-dimensional characteristics are then imported into Simulink to generate and solve the dynamic current equations. The complete modeling procedure is schematically presented in Fig. 3.

The FEM model analysis utilized a cross-section of the motor, as shown in Fig. 4. The materials employed include M-19 electrical steel sheets for the stator

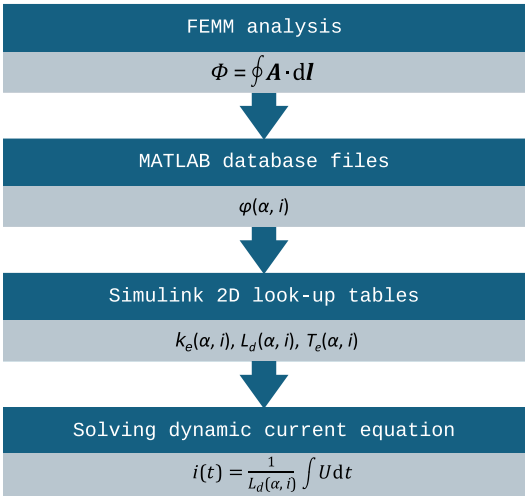

FIG. 3. Schematic diagram of the motor current equation modeling process.

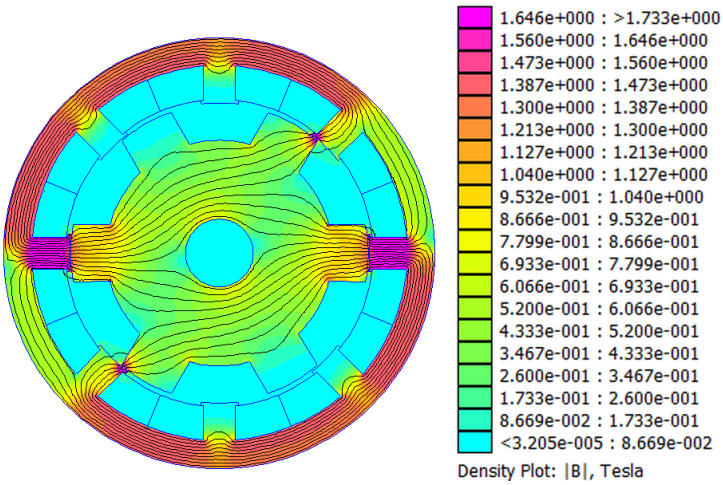

FIG. 4. Magnetic field distributions in the motor cross-section for the coaxial motor position after the post-processing phase of the program.

and rotor (with magnetization characteristics detailed in Fig. 2) and copper for the windings. The motor configuration comprised four phases, eight stator poles and six rotor poles (8/6 configuration). A comprehensive list of all motor parameters is provided in Table 1.

Due to the pole shape's inherent symmetry, calculations for a single phase were sufficient to determine the parameters for the entire motor. In this study, flux values were computed at discrete rotation angles (from 0° to 360° in 1° intervals) across various constant current values (from 0 to 20 A, in 4 A steps).

Table 1. Parameters of the tested reluctance motor.

Motor parameter	Value
Number of phases	4
Number of stator poles	8
Number of rotor poles	6
Number of coils in the winding	70
Motor length	250 mm
Stator outer diameter	117 mm
Air gap length	0.31 mm
Rotor outer diameter	60.79 mm
Shaft diameter	4.73 mm
Stator inner diameter	62 mm
Tooth height	5.5 mm
Tooth tip width	3.5 mm
Tooth foot height	0.5 mm
Tooth width	3 mm
Inner rotor diameter	12.73 mm
Airgap width	3 mm
Airgap height	2.51 mm

The resulting magnetic flux characteristics, expressed as a function of rotor angle and current ($\varphi(i, \alpha)$) formed the basis for subsequent transformations of electromagnetic quantities. Notably, the influence of current in one phase on the flux in another phase was neglected. This assumption is justified by the mutual inductance between concentrated windings on different poles being approximately ten times smaller than the self-inductance of each phase.

2.3. Electromagnetic formulas derivation

This section details the electromagnetic equations that govern SRM operation, forming the basis for the dynamic model.

The voltage induced in a single phase winding k is given by:

$$U_k(i_k\alpha) = \frac{\mathrm{d}\varphi_k(i_k, \alpha)}{\mathrm{d}t}, \tag{2.1}$$

where U_k is the voltage in phase k [V], i_k is the current in phase k [A], α is the rotor angular position [rad], φ_k is the magnetic flux linkage of phase k [Wb], and t is time [s].

Expanding Eq. (2.1) to account for the dependence of the magnetic flux of phase k on both the current and rotor angular position, we obtain:

$$U_k(i_k\alpha) = \frac{\partial\varphi_k(i_k,\alpha)}{\partial i_k}\frac{\mathrm{d}i_k}{\mathrm{d}t} + \frac{\partial\varphi_k(i_k,\alpha)}{\partial\alpha}\frac{\mathrm{d}\alpha}{\mathrm{d}t}. \tag{2.2}$$

In Eq. (2.2), the term $\frac{\partial\varphi_k(i_k,\alpha)}{\partial i_k}\frac{\mathrm{d}i_k}{\mathrm{d}t}$ represents the transformation voltage $U_{kt}\left(i_k,\alpha\right)$ which depends on the temporal variation of the current. The term $\frac{\partial\varphi_k(i_k,\alpha)}{\partial\alpha}\frac{\mathrm{d}\alpha}{\mathrm{d}t}$ denotes the rotation voltage $U_{kr}\left(i,\alpha\right)$, which is proportional to the rotor's angular velocity.

The dynamic inductance of the winding is defined as the partial derivative of the flux with respect to the current:

$$L_k(i\alpha) = \frac{\partial\varphi_k(i,\alpha)}{\partial i_k}, \tag{2.3}$$

where L_k is the dynamic inductance of phase k [H].

Similarly, the induced voltage coefficient of rotation is obtained by differentiating the flux associated with phase k with respect to the mechanical angular position:

$$k_{Ek}(i\alpha) = \frac{\partial\varphi_k(i,\alpha)}{\partial\alpha}, \tag{2.4}$$

where k_{Ek} is the induced voltage coefficient of rotation for phase k [Vs/rad].

Considering the total supply voltage balance in the phase k circuit, $U_k(i_k,\alpha)$, the voltage drop across the total phase resistance R_{tph} (the sum of switch resistance R_s and phase resistance R_{ph}) must be included. Consequently, the complete voltage equation for phase k is:

$$U_k\left(i_k,\alpha\right) = U_{kr}(i\alpha) + U_{kt}(i\alpha) + R_{tph}i_k, \tag{2.5}$$

where U_{kr} is the rotation voltage in phase k [V], U_{kt} is the transformation voltage in phase k [V], and R_{tph} is the total phase circuit resistance [Ω], which is the sum of the switch resistance R_s and phase winding resistance R_{ph}.

Substituting the previously defined terms (Eqs. (2.3) and (2.4)) into Eq. (2.5), the voltage equation for phase k can be expressed as:

$$U_k\left(i_k,\alpha\right) = k_{Ek}\left(i_k,\alpha\right)\frac{\mathrm{d}\alpha}{\mathrm{d}t} + L_k\left(i_k,\alpha\right)\frac{\mathrm{d}i_k}{\mathrm{d}t} + R_{tph}i_k. \tag{2.6}$$

This differential equation involves both electrical (phase current and its time-derivative) and mechanical (rotor's angular velocity) unknowns, alongside parameters such as dynamic inductance, induced voltage coefficient, and total phase resistance.

The electrical equations (Eq. (2.6) for each phase) represent the voltage balance within individual phases. Concurrently, the mechanical equation, presented in Eq. (2.7), establishes the balance of torques. Together, these two equations form the comprehensive mathematical model governing the machine's operation. The mechanical equation determining the electromagnetic torque during the motor operation is given by:

$$T_d + T_D + T_t + T_o = T_e, \tag{2.7}$$

where T_e is the total electromagnetic torque [N · m], T_d is the dynamic torque related to changes in rotor angular velocity (ω) [N · m], T_D is the laminar friction resistance torque proportional to angular velocity [N · m], T_t is the dry friction torque [N · m], T_o is the load torque [N · m], and ω is the rotor angular velocity [rad/s].

To complete the model, the electromagnetic torque T_e must be derived. The co-energy for phase k, denoted as $W'_{mk}(i,\alpha)$, is defined as:

$$W'_{mk}(i,\alpha) = \int_0^{i_k} \psi_k(i'_k,\alpha)\,\mathrm{d}i'_k, \tag{2.8}$$

where W'_{mk} is the magnetic co-energy of phase k [J].

The electromagnetic torque generated by phase k is then given by the partial derivative of the co-energy with respect to the angular position:

$$T_{ek}(i_k,\alpha) = \frac{\partial}{\partial\alpha} W'_{mk}(i_k,\alpha), \tag{2.9}$$

where T_{ek} is the electromagnetic torque from phase k [N · m].

2.4. Magnetic field results

Following the established formulas, differentiation and integration operations of the field functions were performed to calculate the necessary model quantities.

The resulting calculations yielded a matrix of field values φ represented as:

$$\varphi = \begin{bmatrix} \varphi_{11} & \cdots & \varphi_{1j} & \cdots & \varphi_{1n_p} \\ \cdots & \cdots & \cdots & \cdots & \cdots \\ \varphi_{i1} & \cdots & \varphi_{ij} & \cdots & \varphi_{in_p} \\ \cdots & \cdots & \cdots & \cdots & \cdots \\ \varphi_{n_i1} & \cdots & \varphi_{n_ij} & \cdots & \varphi_{n_in_p} \end{bmatrix}. \tag{2.10}$$

In this matrix, n_p denotes the number of elements in the compacted rotor position vector, and n_i represents the number of elements in the compacted current vector. Each row of the matrix corresponds to flux values as a function of rotor position at a constant current value, while each column represents flux values based on current at a specific angular rotor position. The results of these field calculations are presented in Fig. 5, which illustrates that the flux attains its minimum value at the transverse positions (corresponding to the first and last values of the position vector).

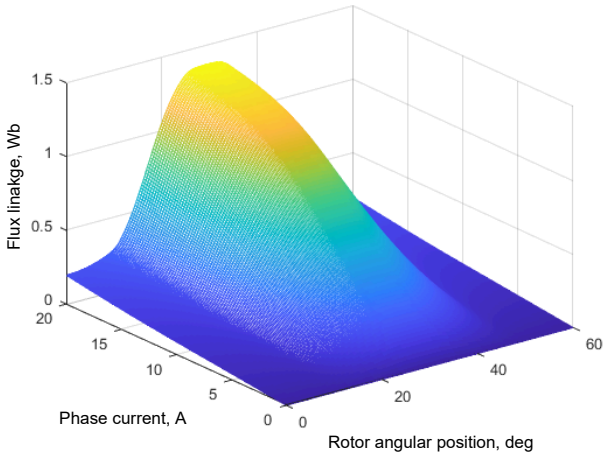

FIG. 5. Schematic diagram of the motor current equation modeling process.

As demonstrated in Fig. 6, the dynamic inductance is a periodic even function that always remains positive, contingent upon the rotor's position. A notable distinction arises between inductance values at the transverse and coaxial

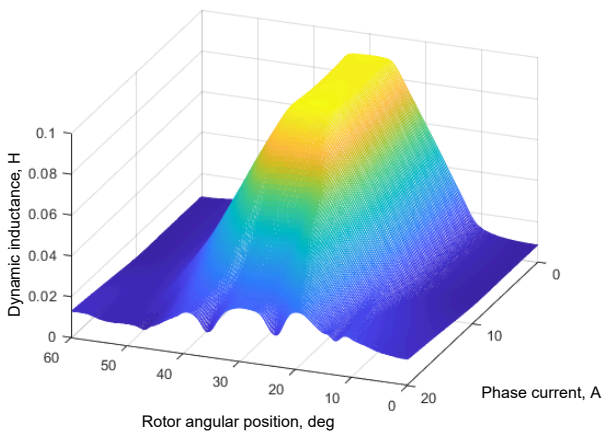

FIG. 6. Dependence of dynamic inductance on current and rotor position.

positions at low current levels. As the current increases, inductance values in the coaxial position decrease, consequently reducing the difference in inductance values across various rotor positions.

Figure 7 shows that, for a given current value, the rotation voltage coefficient, dependent on the rotor position, is a periodic, alternating, odd function. This coefficient is zero at both transverse and coaxial positions for any current value. It takes positive values when the rotor is in the first half of the pole pitch and negative values in the second half. The maximum values of this coefficient increase with increasing currents.

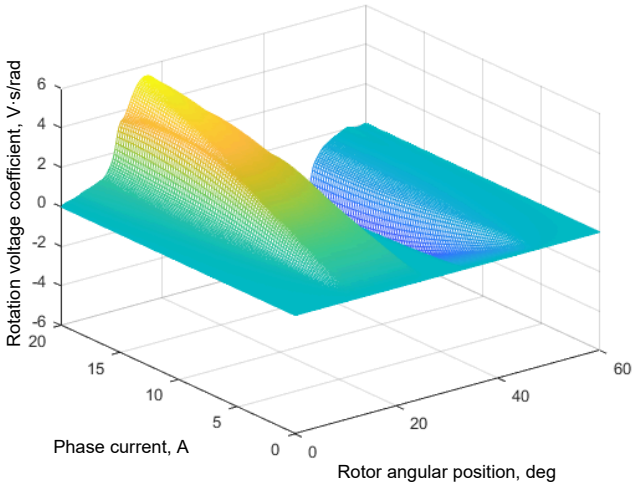

Fig. 7. Dependence of the voltage rotation coefficient on current and rotor position.

To further clarify the dependence of flux, dynamic inductance, and rotation voltage coefficient on both rotor position and current, Fig. 8 presents these functions at selected constant current values. Specifically, these values correspond to the fourth value, every fourth value thereafter up to the penultimate value of the final current vector.

The results of the magnetic co-energy matrix calculations are presented in Fig. 9. At the transverse position (i.e., for the first and last values of the condensed position vector), the magnetic co-energy reaches its minimum value. Consequently, at these positions, the electromagnetic torque can be assumed to be zero for all current values.

Figure 10 illustrates the final form of the electromagnetic torque matrix derived from these calculations.

To provide an even clearer representation of the dependence of flux, magnetic co-energy, and electromagnetic torque on both rotor position and current, Fig. 11 displays these quantities as functions of rotor position at selected con-

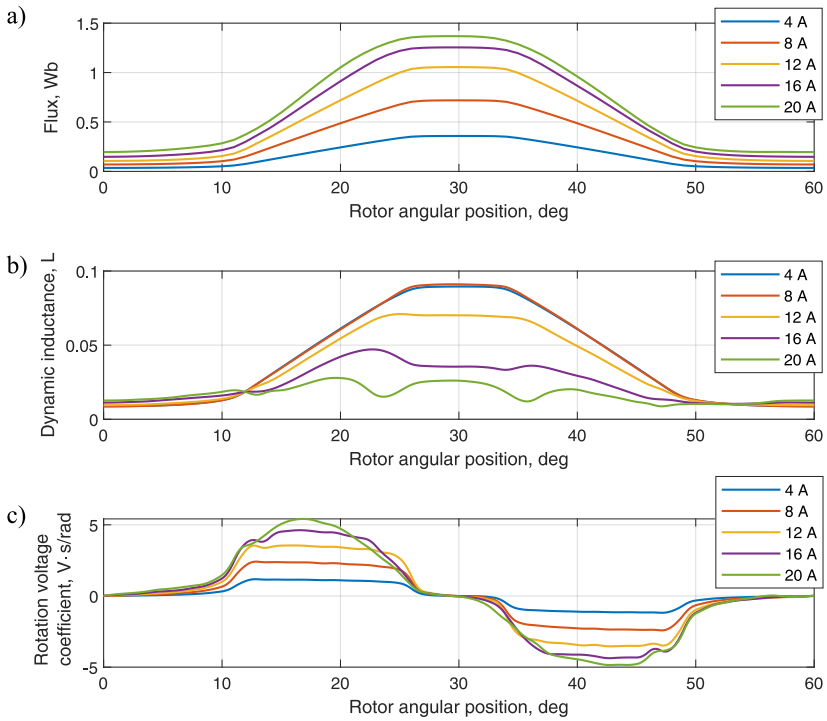

FIG. 8. Dependence of flux (a), dynamic inductance (b), and rotation voltage coefficient (c) on rotor position at selected current values.

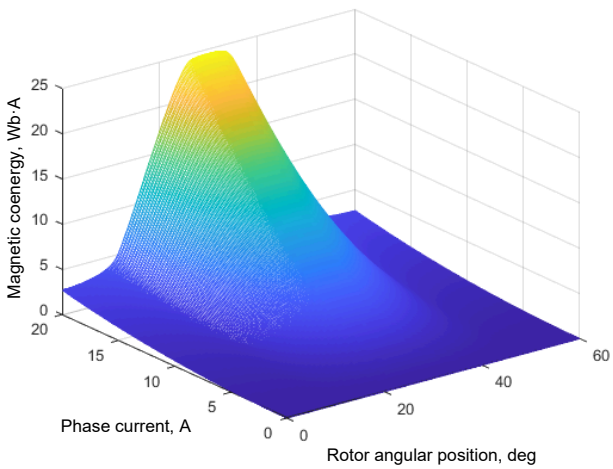

FIG. 9. Dependence of the magnetic coenergy on current and rotor angular position.

stant current values. Specifically starting from the third value, then every second value, up to the penultimate value of the final current vector.

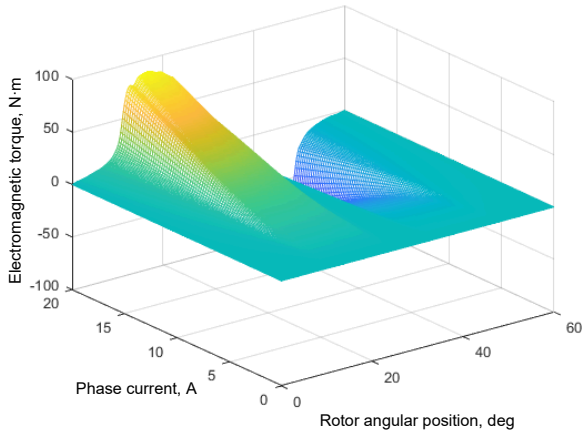

FIG. 10. Dependence of the electromagnetic torque on current and rotor angular position.

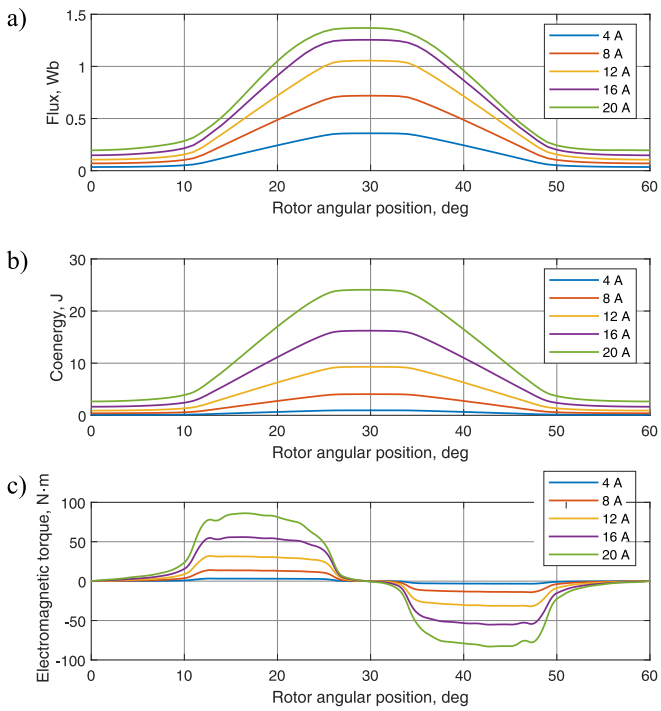

FIG. 11. Dependence of flux (a), coenergy (b), and torque (c) on rotor position at selected current values.

2.5. Eccentricity modeling

Dynamic eccentricity is characterized by a time-varying change in the air gap width, which directly influences the rotor's motion trajectory. Before implement-

ing dynamic equations, it was crucial to conduct magnetostatic measurements under eccentric conditions. To this end, magnetic flux was measured using the FEMM software for each rotor rotation angle along an eccentric path, considering various current values. This process mirrored the methodology used in the previous section for the healthy rotor trajectory. Specifically, the rotor was initially shifted relative to the stator by an eccentricity ϵ equal to 95% of the air gap length. Subsequently, the rotor was rotated along the inner circumference of the stator in 1° increments over a complete 360° rotation (Fig. 12).

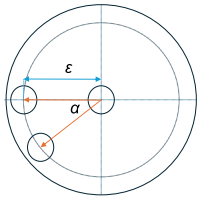

Fig. 12. Illustration of eccentric rotor motion (dimensions not representative of actual size).

As illustrated in Fig. 13, the dependencies of three magnetostatic quantities – flux, dynamic inductance, and rotation voltage coefficient – on the rotor po-

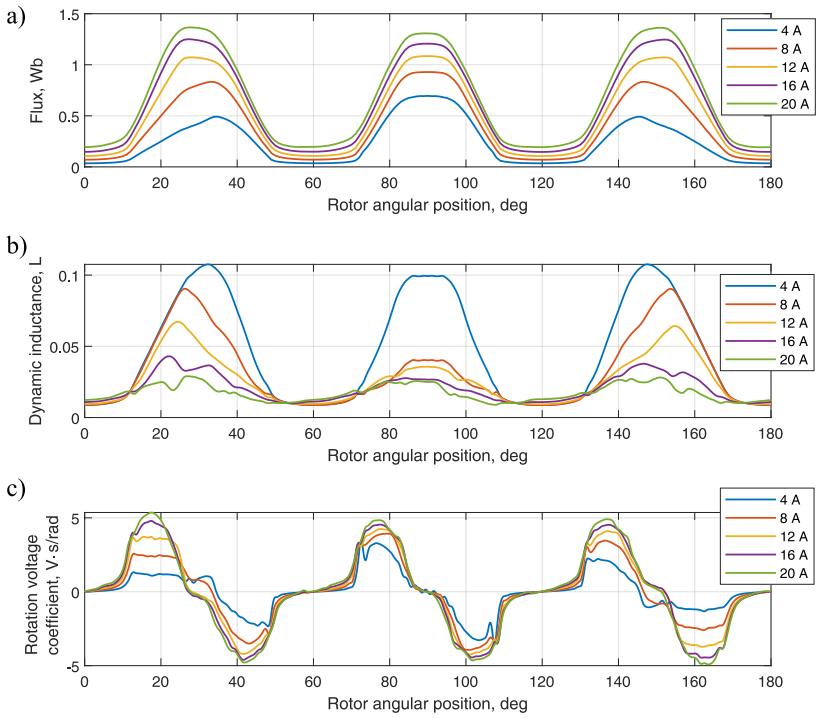

Fig. 13. Dependence of flux (a), dynamic inductance (b), and rotation voltage coefficient (c) on rotor position at selected current values for rotor eccentricity.

sition at selected rotation angles and current values in the eccentric state are analogous to those observed for the healthy motor (discussed in Subsec. 2.4). However, in this case, the displayed rotor rotation range is 180° (three times the pole pitch), rather than just a single pole pitch. For the even-numbered graphs (flux and inductance), maximum values are attained at 90°, while for the odd-numbered graphs (induced voltage coefficient), these maximum values are reached just before and after the inflection point.

A similar trend is observed for co-energy and electromagnetic torque, as presented in Fig. 14, where distinct increases in the maximum values are evident across both the even- and odd-numbered characteristic curves.

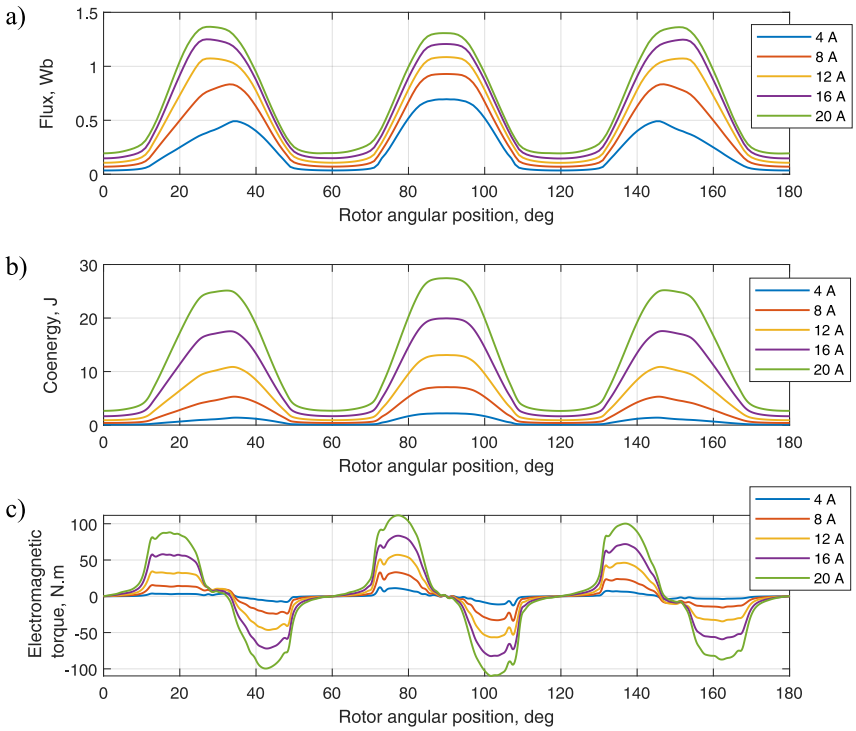

Fig. 14. Dependence of flux (a), coenergy (b), and torque (c) on rotor position at selected current values for rotor eccentricity.

2.6. Dynamic model

For the reluctance machine model in a quasi-static state, the influence of control parameters (contingent on the rotor's angular position and current limits) on operating parameters such as driving torque, efficiency, and torque ripple is investigated. This model assumes a constant rotational speed, representing the condition where electromagnetic torque equals the load torque. This particu-

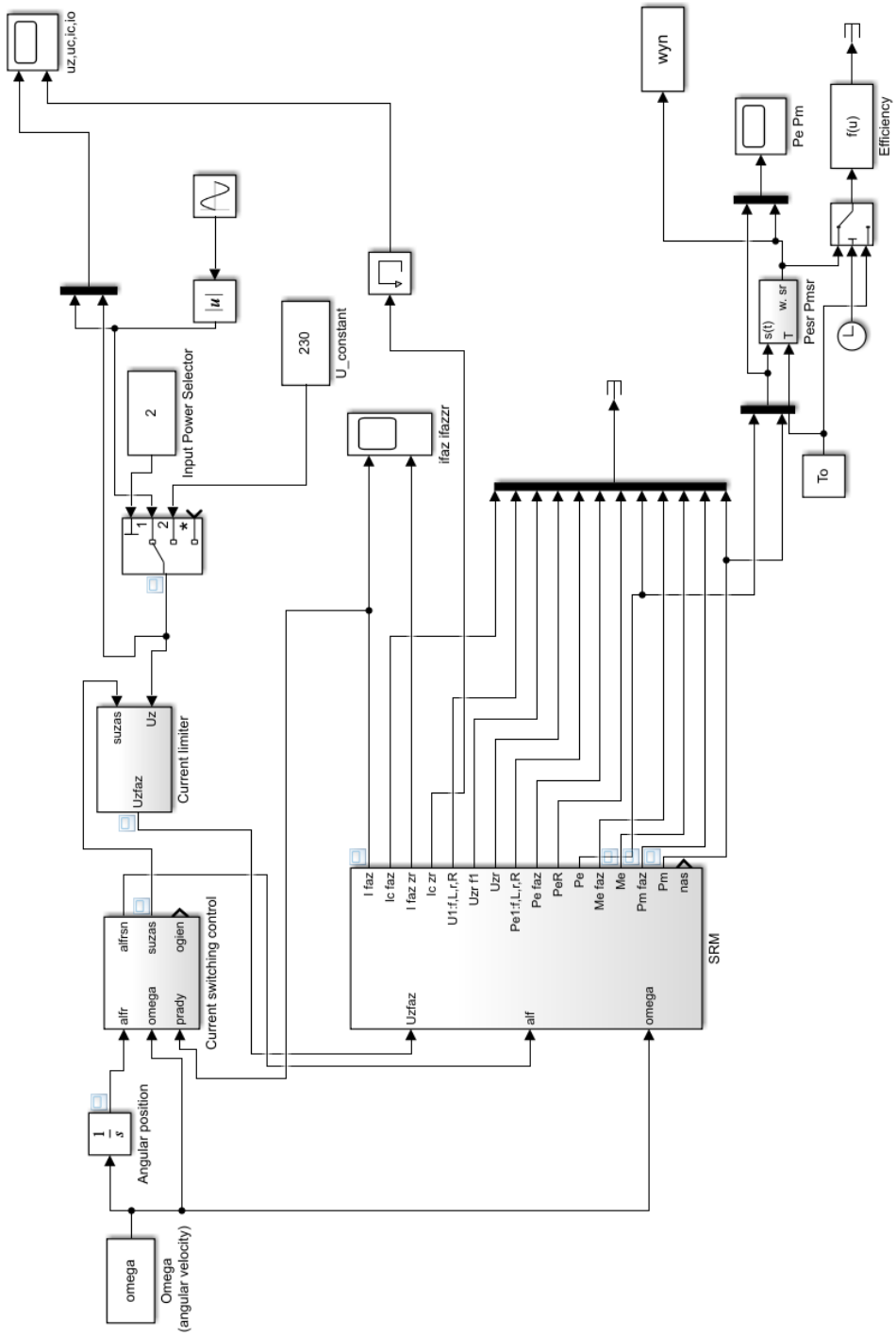

FIG. 15. Dynamic model of the reluctance machine in a quasi-static state.

lar model form does not require additional simplifying assumptions beyond the quasi-static state itself. The comprehensive machine model, detailing all the previously described subsystems, is presented in Fig. 15. The model also includes an automatic simulation termination feature and calculates average values of electrical power, mechanical power, and efficiency under steady-state conditions. The detailed development of this model is thoroughly discussed in Szczypior's study [14].

Simulation results at a rotational speed of 1500 RPM are analyzed in both the time and frequency domains. Figure 16 illustrates the time-domain waveforms of the motor current under various eccentricity conditions, including normal operation and eccentricity levels of 25%, 50%, 75%, and 90%. Each subplot within

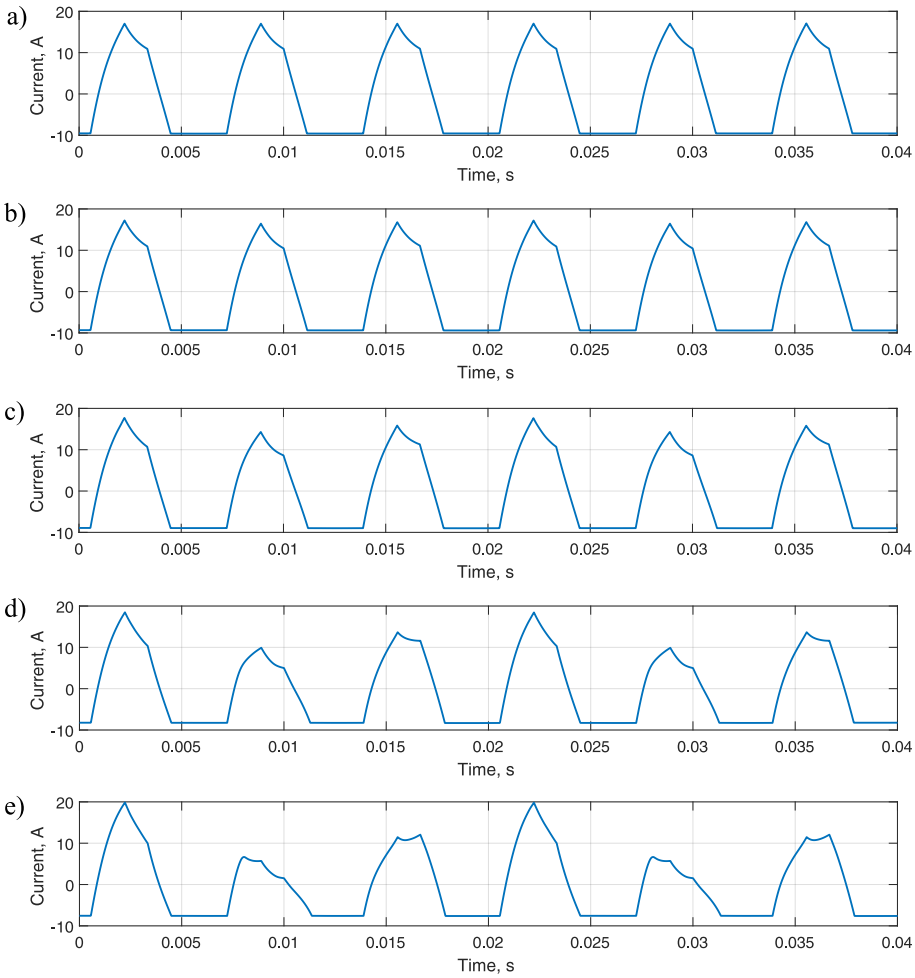

Fig. 16. Current pulses over time for motor operating conditions. Time waveform for: a) normal operation, b) 25% eccentricity, c) 50% eccentricity, d) 75% eccentricity, e) 90% eccentricity.

Fig. 16 displays current in amperes over a 0.04-second interval. Under optimal operating conditions, the six current pulses per mechanical rotation exhibit a uniform shape. However, as eccentricity increases, a visible distortion and modulation of the current waveform become progressively more pronounced. This phenomenon, attributable to the varying air gap length and subsequent inductance variations for each current pulse, directly correlates the severity of motor eccentricity with the deformation of the current signal in the time domain, serving as a preliminary indicator for motor health assessment.

Figure 17 displays the amplitude spectra of the motor current under the same varying eccentricity conditions (25%, 50%, 75%, and 90% eccentricity). Each subplot highlights the frequency content up to 300 Hz, with vertical dashed

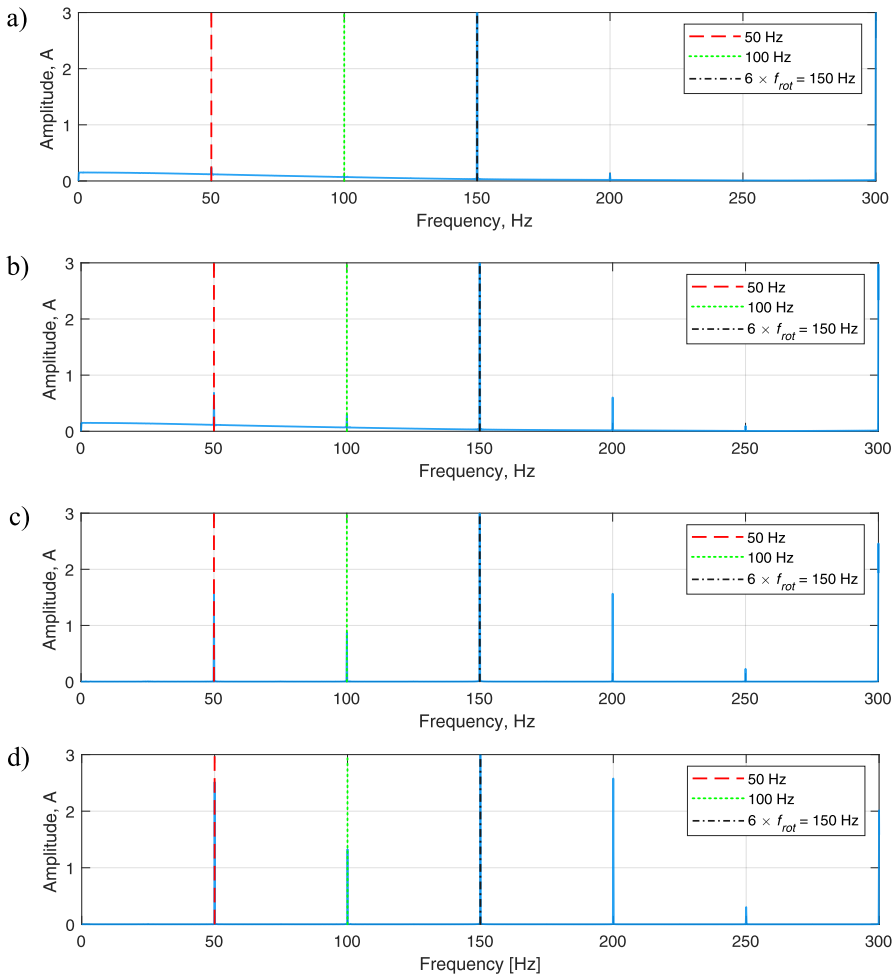

Fig. 17. Motor current amplitude spectra for eccentricity conditions: a) 25%, b) 50%, c) 75%, d) 90%.

lines indicating key frequencies at 50 Hz, 100 Hz, and 150 Hz (corresponding to $6\,f_{rot}$). Under optimal motor operation, harmonics are observed at approximately 150 Hz intervals (corresponding to the sixth multiple of the rotational speed, $6 \cdot 25$ Hz), thereby validating the accuracy of the results. In the event of eccentricity fault, additional harmonics distinctly emerge at 50 Hz (representing twice the mechanical rotation cycle, i.e., $2\,f_{rot}$) and its higher multiples. As the level of eccentricity increases from 25% to 90%, a noticeable rise in the amplitudes of sideband frequencies, particularly around 100 Hz and 200 Hz (seen as growing peaks next to the main 150 Hz component), can be observed. This progressive increase in sideband amplitudes directly correlates with the severity of the eccentricity, confirming the diagnostic value of spectral analysis for identifying and quantifying mechanical faults within the motor. At higher frequency range, the amplitudes of these harmonics decrease to zero.

Figure 18 presents a quantitative comparison of the amplitudes of key current harmonic components (50 Hz, 100 Hz, 200 Hz, and 250 Hz) across different levels of motor eccentricity: 25%, 50%, 75%, and 90%. Each group of bars represents a distinct eccentricity level, with individual bars indicating the amplitude (in amperes) of specific harmonics. A clear trend of increasing amplitudes for the 100 Hz and 200 Hz harmonics is observed as eccentricity increases from 25% to 90%. This consistent increase underscores the diagnostic value of these specific harmonic amplitudes as reliable indicators for quantifying the severity of rotor eccentricity in electrical machines. Additionally, the 50 Hz amplitude

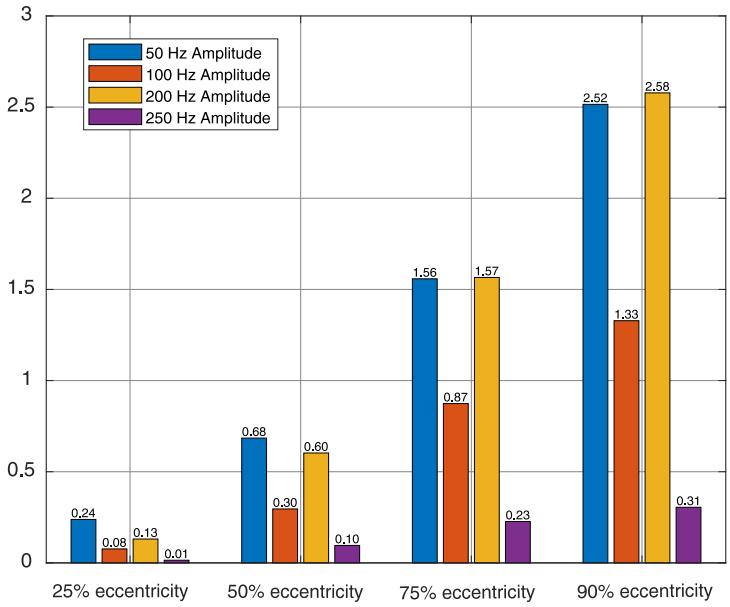

Fig. 18. Amplitudes for different eccentricity conditions.

shows a significant increase, reflecting the impact of eccentricity on the fundamental component.

3. Summary

This study unequivocally demonstrates the multifaceted impacts of dynamic rotor eccentricity on the motor's current signal through a comprehensive analysis encompassing time-domain waveforms, amplitude spectra, and a comparative evaluation of harmonic amplitudes. Visual examination of the current waveforms reveals progressive distortion and modulation of the otherwise sinusoidal signal as eccentricity increases, establishing a clear correlation between fault severity and the current's temporal behavior. This deformation is quantitatively supported by frequency-domain analysis, which shows the distinct emergence and significant amplification of specific sideband frequencies, particularly around 100 Hz and 200 Hz, adjacent to the fundamental and primary harmonic components.

Further quantitative comparisons underscore the escalating magnitudes of these specific harmonic amplitudes with increasing eccentricity. Specifically, the 100 Hz amplitude showed substantial increases relative to the 25% eccentricity baseline: approximately 286.16% for 50% eccentricity, 1040.73% for 75% eccentricity, and 1634.20% for 90% eccentricity. Similarly, the 200 Hz amplitude exhibited significant growth of about 360.50% for 50% eccentricity, 1096.03% for 75% eccentricity, and 1869.44% for 90% eccentricity for the same 25% eccentricity baseline.

Collectively, these findings establish current signature analysis as a robust and highly sensitive method for detecting and quantifying rotor eccentricity in electric motors. This method provides consistent and correlative indicators in both the time and frequency domains, precisely reflecting the severity of the mechanical fault.

The inherently nonlinear magnetization characteristics of reluctance motors, which necessitate the implementation of the FEM combined with dynamic equation solutions, pose significant challenges in their study. The introduction of additional factors such as eccentricity further complicates this analytical approach. Nevertheless, the models developed in this study yielded promising results, demonstrating that dynamic eccentricity causes an uneven distribution of the magnetic field within the motor, leading to distinct and observable alterations in the phase current characteristics. It is essential for users of these motors to recognize these signal alterations, as they serve as critical indicators of adverse operating conditions.

This study significantly contributes to the body of research conducted at the test station [15, 16], providing a solid foundation for future diagnostic analy-

ses of SRMs. Further research could explore the application of this method to experimental data and real-time monitoring and fault detection systems.

References

1. Bilgin B., Jiang J.W., Emadi A., *Switched Reluctance Motor Drives: Fundamentals to Applications*, CRC Press, Boca Raton, FL, 2018.
2. Husain I., Switched reluctance machines, [in:] *The Power Electronics Handbook*, Rashid M.H. [Ed.], pp. 879–933, CRC Press, Boca Raton, FL, 2018.
3. Biernat, A., *Analysis of diagnostic signals of electrical machines* [in Polish: *Analiza sygnałów diagnostycznych maszyn elektrycznych*], Oficyna Wydawnicza Politechniki Warszawskiej, Warszawa, 2015.
4. Toliyat H.A., Ghahramani M., Karami N., *Electric machines: modeling, condition monitoring, and fault diagnosis*, CRC Press, Boca Raton, FL, 2017.
5. Hu Y., Zhang Z., Sun D., Gu C., Li Y., Fault diagnosis of full-bridge power converter for SRMs based on modified current detection, *IEEE Journal of Emerging and Selected Topics in Power Electronics*, **12**(3): 1042–1053, 2024, https://doi.org/10.1109/JESTPE.2023.3345410.
6. Ali N., Wang Q., Gao Q., Ma K., Diagnosis of multicomponent faults in SRM drives based on auxiliary current reconstruction under soft-switching operation, *IEEE Transactions on Industrial Electronics*, **71**(3): 2265–2276, 2024, https://doi.org/10.1109/TIE.2023.3266596.
7. Zhang L., Song J., Wang X., Lu J., Lu S., High-resistance connection fault diagnosis of SRM based on multisensor calibrated transformer with shifted windows, *IEEE Sensors Journal*, **23**(24): 30971–30983, 2023, https://doi.org/10.1109/jsen.2023.3331695.
8. Xing C., Zhu Y., Wang J., Wu H., Huang Y., Coordination control between vibration suppression and energy regeneration for vehicles driven by in-wheel motors under regenerative braking condition, *Proceedings of the Institution of Mechanical Engineers, Part D: Journal of Automobile Engineering*, **239**(2–3): 847–865, 2023, https://doi.org/10.1177/09544070231208161.
9. Rani S., Jayapragash R., FEA-based pole arc optimization and sensitivity analysis of 8/6 SRM for EV application, *Results in Engineering*, **23**: 102683, 2024, https://doi.org/10.1016/j.rineng.2024.102683.
10. Lorencki J., Radkowski S., Gontarz S., Diagnostically oriented experiments and modelling of switched reluctance motor dynamic eccentricity, *Sensors*, **21**(11): 1–13, 2021, https://doi.org/10.3390/s21113857.
11. Lorencki J., Radkowski S., Mechanical faults analysis in switched reluctance motor, *Applied Sciences-Basel*, **14**(8): 1–16, 2024, https://doi.org/10.3390/app14083452.
12. Torkaman H., Afjei E., Magnetostatic field analysis and diagnosis of mixed eccentricity fault in switched reluctance motor, *Electromagnetics*, **31**(5): 368–383, 2011, https://doi.org/10.1080/02726340902953354.
13. Faiz J., Pakdelian S., Diagnosis of static eccentricity in switched reluctance motors based on mutually induced voltages, *IEEE Transactions on Magnetics*, **44**(8): 2029–2032, 2008, https://doi.org/10.1109/TMAG.2008.2001648.

14. Dorrell D.G., Cossar C., A vibration-based condition monitoring system for switched reluctance machine rotor eccentricity detection, *IEEE Transactions on Magnetics*, **44**(9): 2204–2207, 2008, https://doi.org/10.1109/TMAG.2008.2001389.

15. Torkaman H., Afjei E., Yadegari P., Static, dynamic, and mixed eccentricity faults diagnosis in switched reluctance motors using transient finite element method and experiments, *IEEE Transactions on Magnetics*, **48**(8): 2254–2260, 2012, https://doi.org/10.1109/TMAG.2012.2195977.

16. Szczypior J., Bieńkowski K., Mathematical model of a switched reluctance motor [in Polish: Model matematyczny silnika reluktancyjnego przełączalnego], [in:] *Prace IX Sympozjum Symulacja Procesów Dynamicznych SPD-9*, pp. 257–263, Polana Chochołowska, 1996.

Received February 10, 2025; accepted version June 30, 2025.
Online first August 13, 2025.